Unearthing real-time 3D ant tunneling mechanics

Robert Buarque de Macedo[a], Edward Andò[b], Shilpa Joy[a], Gioacchino Viggiani[b], Raj Kumar Pal[c], Joseph Parker[d], and José E. Andrade[a,1]

[a]Department of Mechanical and Civil Engineering, Caltech, Pasadena, CA 91125; [b]Université Grenoble Alpes, Institut Polytechnique de Grenoble, Sols, Solides, Structures, Risques (3SR), CNRS, F-38000 Grenoble, France; [c]Mechanical and Nuclear Engineering Department, Kansas State University, Manhattan, KS 66506; and [d]Division of Biology and Biological Engineering, Caltech, Pasadena, CA 91125

Edited by David A. Weitz, Harvard University, Cambridge, MA, and approved July 18, 2021 (received for review February 8, 2021)

Granular excavation is the removal of solid, discrete particles from a structure composed of these objects. Efficiently predicting the stability of an excavation during particle removal is an unsolved and highly nonlinear problem, as the movement of each grain is coupled to its neighbors. Despite this, insects such as ants have evolved to be astonishingly proficient excavators, successfully removing grains such that their tunnels are stable. Currently, it is unclear how ants use their limited information about the environment to construct lasting tunnels. We attempt to unearth the ants' tunneling algorithm by taking three-dimensional (3D) X-ray computed tomographic imaging (XRCT), in real time, of *Pogonomyrmex* ant tunnel construction. By capturing the location and shape of each grain in the domain, we characterize the relationship between particle properties and ant decision-making within an accurate, virtual recreation of the experiment. We discover that intergranular forces decrease significantly around ant tunnels due to arches forming within the soil. Due to this force relaxation, any grain the ants pick from the tunnel surface will likely be under low stress. Thus, ants avoid removing grains compressed under high forces without needing to be aware of the force network in the surrounding material. Even more, such arches shield tunnels from high forces, providing tunnel robustness. Finally, we observe that ants tend to dig piecewise linearly downward. These results are a step toward understanding granular tunnel stability in heterogeneous 3D systems. We expect that such findings may be leveraged for robotic excavation.

tunneling | granular mechanics | ants | robotics | applied physical sciences

Excavation is a vital component of both the natural world and modern civilization. Mining alone constitutes an over $80 billion industry nationally (1), providing an abundance of materials upon which society relies. In nature, insects such as ants have evolved strategies for large-scale efficient and durable tunnel excavation. Indeed, colonies of subterranean-nesting ant species can create nest structures several meters in depth that can persist for decades (2). This biological feat of engineering has fascinated both biologists and physicists alike (3–5) but is especially captivating from a mechanics perspective (6). As anyone who has played Jenga is aware (7), removing certain blocks is more likely to cause a collapse than removing others. What principles do ants follow such as to avoid removing structurally critical grains during excavation? Do factors other than safety determine digging technique (i.e., time and energy efficiency)? Do ants dig according to a simple, innate algorithm? By studying termite mounds, robots following termite-inspired algorithms have been implemented for autonomous construction (8). Similarly, understanding the innate, collective behavior algorithm that ants employ to excavate tunnels could lead to more efficient and economical digging strategies for resource extraction. Mining collapses can cost up to $100 million individually (9), in addition to threatening the safety of the workers. Eventually, an autonomous mining robot following said methodology may allow humans to avoid dangerous excavations altogether (10). Such a robot is ideal for interplanetary mining (11), adapting to extreme and changing conditions before a terrestrial human receives a signal.

There exists a rich body of literature investigating the mechanics and structure of ant tunnels. Classically, the three-dimensional (3D) forms of subterranean colonies were elucidated by the pouring of coagulating fluids into an unoccupied (or euthanized) colony. These landmark studies revealed the ordered chaos of the ant underworld: a byzantine collection of vertical or angled tunnels coalescing about horizontal chambers (2, 12). By contrast, inferring how such structures were created by the ants has typically relied on the use of far simpler, often two-dimensional (2D) experimental nests. For example, the effects of soil grain size distribution and saturation on tunneling diameter, stability, and structure were studied by observing quasi-2D ant farms housing harvester ants (*Pogonomyrmex barbatus*) (6). For this species, it was shown that the most effective tunnel excavation was observed when grains were small enough such that workers could carry particles with their mandibles. Yet, cohesion had to be high enough to support tunnel structures but not so much as to resist the ants' pulling force. In another 2D study, it was found that the area and digging rate of excavation depended on the size of the fire ants involve. However, the topological structure of the tunnels (i.e., the ratio of edges to vertices in a graph representation of the tunnel) was independent across ant size scales (13). To elucidate features of the ant digging algorithm that lead to robust tunnel formation, there is a critical need to both quantify how ants tunnel in three dimensions and

Significance

Predicting the stability of granular materials under particle removal has wide-reaching applications, including automating tunnel excavations. Searching for general laws that govern granular stability is challenging given the complexity of granular material dynamics. However, knowledge may be gained from the natural world, where organisms have evolved adaptive tunneling strategies. Among these, subterranean-nesting ants execute an innate tunneling behavioral program that can lead to remarkably stable tunnel excavation. We use X-rays to image the process of ant tunnel construction through a particulate substrate. We use these data to create a grain-scale accurate simulation for estimating particle mechanics in the sample during real-time excavation. We present evidence that ants benefit from force redistributions during incremental digging, suggesting techniques for robotic mining.

Author contributions: E.A., S.J., G.V., and J.E.A. designed research; R.B., S.J., R.K.P., and J.E.A. performed research; R.B., E.A., G.V., and R.K.P. analyzed data; and R.B. and J.P. wrote the paper.

The authors declare no competing interest.

This article is a PNAS Direct Submission.

[1]To whom correspondence may be addressed. Email: jandrade@caltech.edu.

This article contains supporting information online at https://www.pnas.org/lookup/suppl/doi:10.1073/pnas.2102267118/-/DCSupplemental.

Published August 23, 2021.

deduce how their actions impact the mechanical properties of the surrounding soil.

Nowadays, 3D X-ray computed tomographic imaging (XRCT) offers a potential solution for nondestructive analysis of 3D colonies. Minter et al. (14) leveraged such technology to demonstrate how ants will change digging angle when encountering gradients in soil density. Gravish et al. (15) tracked tunnel diameter via XRCT, illustrating how tunnel size is correlated with worker ant morphology, in particular body length. Goldman and coworkers (16) utilized 3D XRCT images of ant tunnels at multiple instances in time to demonstrate how increasing water content at low to intermediate moisture levels correlates with the properties of tunnels dug by ants. By measuring the yield force required to drag a rod on a robotic arm through the soil, it is discovered that increases in yield force due to moisture content correlate with increasing tunnel depth. This work suggests that soils with higher yield strengths lead to more robust and stable tunnels. Computer simulations have also emerged as a means for probing ant tunnel mechanics. Frost et al. (3) employed discrete element method (DEM) simulations (17)—which model grains as rigid objects obeying Newtonian physics—to discover that soil arching around rectangular cavities increases the stability of surrounding openings, a possible explanation for interwoven tunnel geometries. Behaviorally, ants follow patterns when selecting grains for wall construction, exhibiting a preference for heterogeneous grain sizes. Such a mixture will have a higher angle of repose and therefore, stability than homogeneous collections of grains (18). Furthermore, ants will prioritize ease of grain removal when digging over robustness of the resulting wall (19). Clearly, ant tunnel construction is strongly influenced by the granular makeup of the soil. Nevertheless, it remains unclear how exactly ants construct stable tunnels in natural settings.

Unsaturated soils, like most granular materials, exhibits "force chains," which are networks of particles carrying the majority of stress (20, 21). As mentioned in ref. 3, removing particles in these chains is likely to provoke instability, in addition to being harder to remove due to frictional resistance. Do ants avoid extracting grains from such chains? More so, if the increase of interparticle forces leads to more robust tunnels, how do ants cope with the increasing energetic cost of grain removal (16)? These questions are key toward the development of a bio-inspired tunneling algorithm that minimizes the probability of collapse.

In this study, we employ 3D XRCT to map the forces around real ant tunnels during naturalistic tunnel construction. We use this mapping to explore patterns relating tunnel construction to force distributions in real time, in addition to other critical granular material attributes. Because the shape, position, and orientation of grains are crucial for determining force distributions in a soil (22–25), we consider grain-scale properties of the excavated soil and their evolution in time. With XRCT, we achieve submillimeter-resolution 3D imaging on a frustum-shaped container of ants and soil during tunnel excavation. Leveraging these data, we recreate the experiments in silico via a DEM simulation, which can model particles of arbitrary shapes—the level set discrete element method (LS-DEM) (26). From this simulation, we calculate the changing temporal dynamics of interparticle and grain-wall forces throughout the entire sample as ants execute their tunneling behavioral program. This combination of high-resolution dynamic imaging of tunnel excavation complemented by grain-scale mechanics unveils the spatiotemporal mesoscopic impact of tunneling ants on the surrounding substrate, elucidating why ants are such efficacious tunnellers.

Methods

To probe the effect of granular physics on ant tunneling behavior, we leverage XRCT imaging at submillimeter resolution. Five hundred milliliters of Quikrete soil with average grain diameter of 2.3 mm (*SI Appendix*) was mixed with 20 mL of water and poured into the frustum for a water content $\omega = 0.03$ and initial porosity of 0.42. The frustum was encapsulated into a device specifically designed for our XRCT experiments (*SI Appendix*). The device was placed into a computed tomography scanner, and a 40-min high-resolution scan was performed of the entire sample. Fifteen *Pogonomyrmex occidentalis* ants were released into the top of the container, and the container was sealed (27). *Pogonomyrmex* ants were chosen because of their prolific digging ability to handle grains on the millimeter scale, such as those used in the experiment that are ideal for XRCT imaging. Fifteen ants were chosen through an optimization procedure performed using the same species of ant and soil as the main experiment. Starting from one ant, increasing numbers of ants were observed digging through soil in a laboratory environment. It was found that the optimal excavation rate was achieved starting at 15 ants. Following this, faster (4-min) half-resolution scans were taken every 10 min over the course of about a day. Each scan captured the structure and orientation of almost all particles in the sample in 3D. Six instances of the experiment were performed overall, although due to the machine occasionally pausing overnight (*SI Appendix*), only three studies collected continuous data on ant tunneling. While the morphology of all three experiments is studied, the first two experiments are primarily analyzed in this article, as they span the two possible cases of tunnels on the boundary and in the bulk.

From these 3D images, a digital avatar was created for each particle in the sample. As explained in *SI Appendix*, a particle avatar is a mathematical representation of a grain's shape, position, and orientation, factors known to significantly influence force distribution (28). Furthermore, by comparing images taken at different instances in time, the order of grain removal by the ants could be determined—up to the frequency of the scans. From here, the morphological properties of removed grains and kept grains were compared, and an LS-DEM simulation utilizing these avatars was executed. All four steps of the digital reconstruction are illustrated in Fig. 1 (29).

Results and Discussion

Tunnel and Particle Morphology. Tunnel and grain shape properties were analyzed before considering force chains to probe the mechanics at the tunnel scale. Splines were fit to tunnels for obtaining a smooth representation of the tunnel axes. In Fig. 2, *Upper*, a depiction of the spline—with tunnel axis direction obtained from the spline gradient—is presented for the three successful experiments. Fig. 2, *Lower* shows multiple measures for quantifying the tunnel's structure.

Ants tend to dig on the container's boundary; in all cases, the initial tunnel began from the container's boundary. Of all five tunnels pictured, only one tunnel (green) passes through the interior during descent. This predilection for the boundary could be simply a matter of geometry; ants start digging down after horizontal motion is inhibited (e.g., by the container's boundary). Or, it could be due to the difference in cohesion between the container's boundary and the particles compared with particle–particle interactions. The latter explains why ants tend to stick to the boundary during excavation.

The ants tend to dig in linear segments. Specifically, along piecewise segments, the ants maintain an approximately constant digging angle ϕ (defined as the angle of the tunnel axis with respect to a horizontal plane). This can be seen in all five of the tunnels. However, the purple and blue tunnels do show gradual variation in angle in parts. Almost vertical descents occur at the top. In the bulk, ants dig at or below the angle of repose for the material ($\approx 40^\circ$) (*SI Appendix*). Yet, as pointed out above, the ants exploit the presence of boundaries where they can reach higher digging angles ϕ, such as in experiment 3 (purple/blue). This quantitative measure of digging angles in a cohesive material is consistent with qualitative observations in ref. 6.

The aspect ratio of the tunnel is calculated at each point along the spline. At a given spline point, a plane is defined with normal vector in the direction of the spline, passing through the spline point. All particles which intersect this plane are identified, and the location of their centroid before removal is

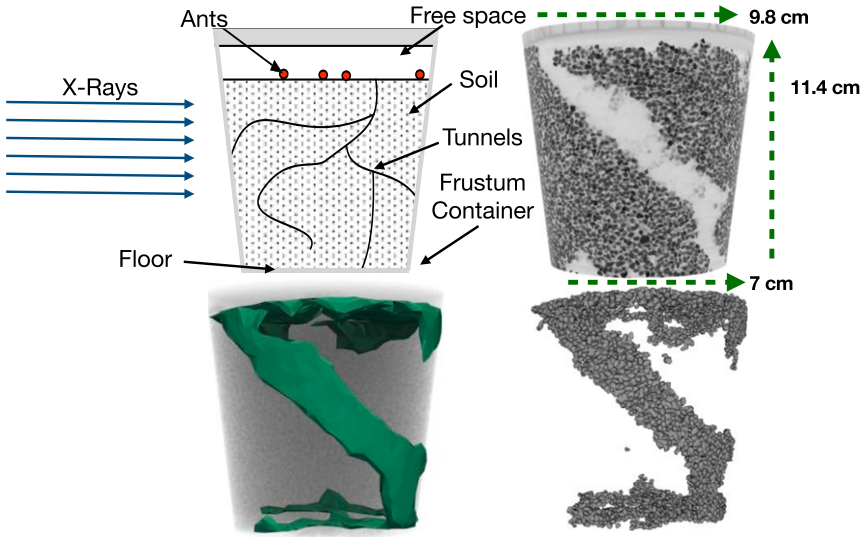

Fig. 1. (*Upper Left*) Experimental design. (*Upper Right*) One viewpoint of a completed tunnel from X-ray imaging. (*Lower Left*) The α-shape fit to the locations of removed particle centroids for viewing the 3D tunnel, with $\alpha = 40$ (29). (*Lower Right*) Digital recreation of particles removed by ants in initial location.

recorded. Principal component analysis was performed on the centroids projected into this plane, and the ratio of the largest to smallest eigenvalue was taken as the tunnel aspect ratio. After a tunnel is born from the top excavation, tunnel diameter and aspect ratio are mostly constant, with the green and red tunnels having the lowest aspect ratios and diameters (approximately four times the particle diameter; consistent with ref. 15). For tunnels dug against a boundary, tunnel morphology

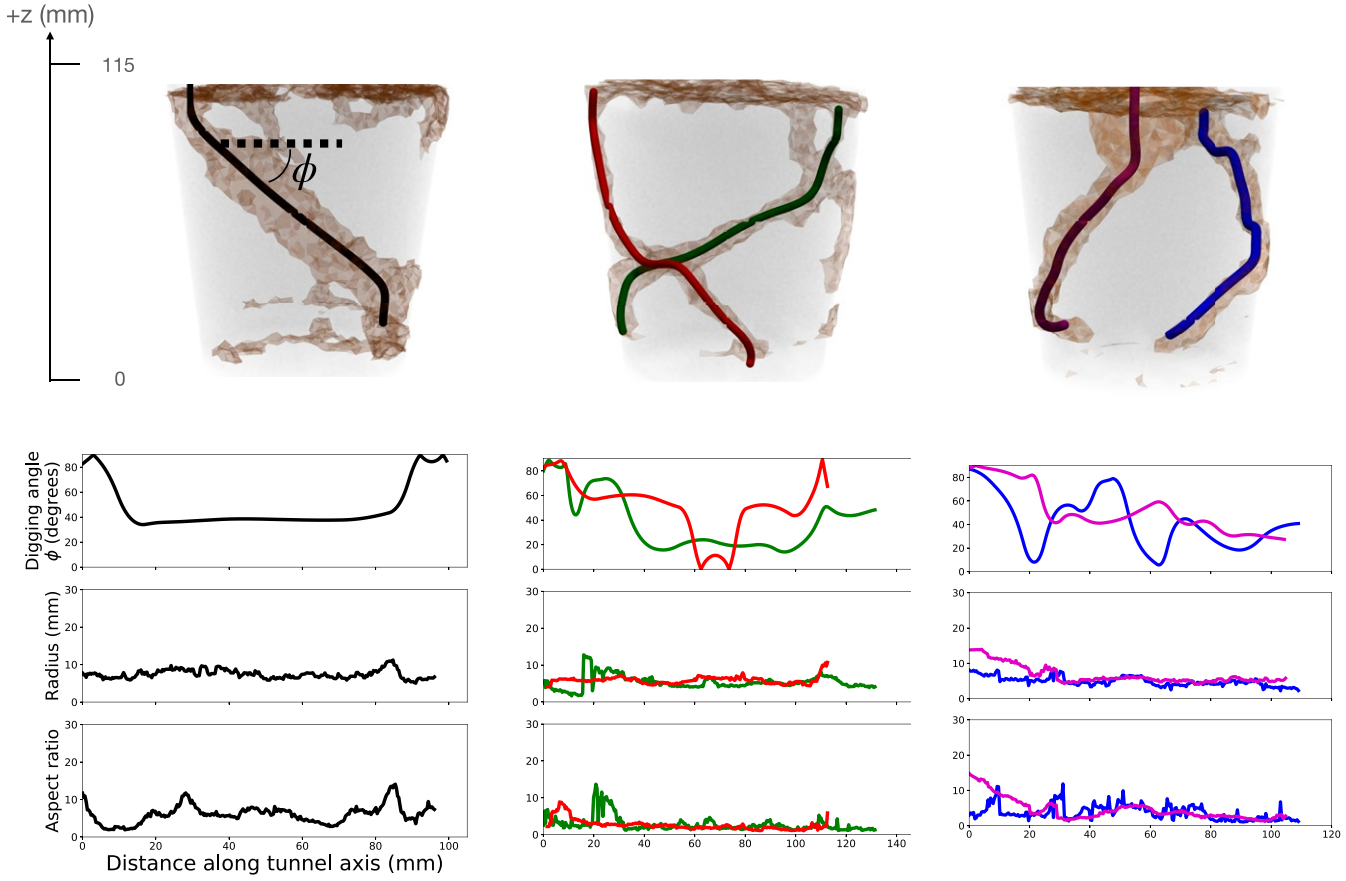

Fig. 2. (*Upper*) Interpolating spline fit to an ant tunnel, with scale for height. (*Lower*) Digging angle to horizontal plane ϕ, tunnel radius, and aspect ratio as a function of distance along tunnel axis obtained from splines. High-resolution images of the three experiments with splines are in *SI Appendix*, Figs. S4–S8.

is elliptical, raising the cross-section aspect ratio. This shape could be the result of ants excavating a segment of a circular tunnel.

The high-resolution scan's voxel edge length (70 μm) is about $\frac{1}{40}$ of average particle diameter. This level of detail for each grain means that the ants' preferences for removing particles with certain attributes can be explored. The volume of the grains has been quantified by counting the number of voxels in each particle via the spam python library. The distributions of volume between removed and nonremoved particles are compared for statistical significance using a Kolmogorov–Smirnov test (*SI Appendix*, Fig. S2). There appears to be a slight, yet statistically significant, bias for lower-volume grains. This result is consistent with experiments in ref. 6, in which ants prefer to remove particles with diameter comparable with mandible size (1 to 2 mm).

Mechanics of Tunnel Surface. The forces localized on the tunnel surface are studied in this section, offering insight into ant tunneling behavior. Multiple forces exist between adjacent grains in an unsaturated granular material. At the scale of our particles ($\approx 10^{-3}$m), the dominating forces are cohesion, friction, weight, and contact between grains and with walls (6, 30). To calculate these forces, we leverage LS-DEM, detailed in *SI Appendix*. In summary, we begin with a digital twin of the experiment. This means that each particle in the original physical frustum maps to a computational particle as illustrated in Fig. 1, *Lower Right*. The digital particles match the physical grains up to the resolution of the scans—0.07 mm. This resolution is sufficient to capture the shape, orientation, and position of the particles (*SI Appendix*, Fig. S1). The precise reproduction of each interparticle contact in LS-DEM may not match reality exactly. Indeed, even if we matched the contacts precisely, we could not guarantee an exact reconstruction of the forces due to the indeterminate nature of force chains (31). Further, we could not image the location and shapes of all the liquid bridges. Nonetheless, we are more interested in capturing the general behavior of forces in our sample—such as the dependence of force chain morphology on the growth of the tunnel. This emergent behavior is more dependent on the distribution of particle shapes and boundary conditions than on the specific contact locations (22, 32). In this regard, LS-DEM has shown high efficacy (33).

The DEM simulation of these grains is left to equilibrate under the aforementioned forces. Cohesion is handled in our simulation using the bond model developed in ref. 34. Details on this model are given in *SI Appendix*. Grains are then deleted in the order in which ants removed the particles. Since scans were performed every 10 min, many grains (≈ 100) are removed during each scan. After every round of particle removal, an equilibration is performed. This methodology is similar to that of dissolution studies (35). We number each equilibration chronologically, denoting this number as the experiment's "frame."

The structures of forces for experiments 1 and 2 were analyzed. Fig. 3 depicts particles and simulated forces from experiment 1. Fig. 3, *Upper* displays the system of particles at a particular frame, while Fig. 3, *Lower* corresponds to a temporally later frame (70 min later). In the first column, the X-ray image is displayed, with particles on the tunnel's surface rendered individually. Particles that will be removed in the immediate next frame are shaded. Column 2 illustrates the forces between particles on the tunnel surface for the two frames. Each black line is a branch vector (i.e., a vector that connects the center of masses between two interacting particles). The thickness of the line is proportional to the magnitude of the normal force between the participating grains. Branches of contiguous particles woven together by high

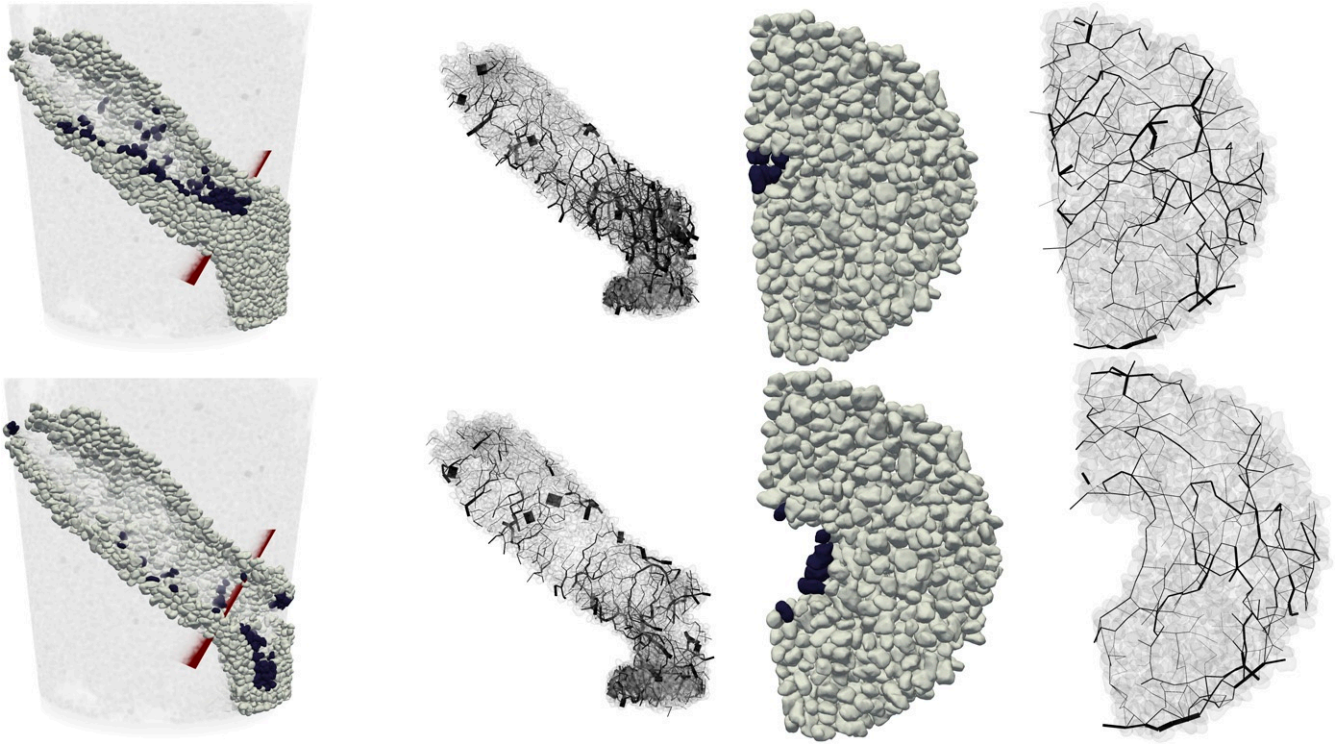

Fig. 3. Visualization of forces on grains in and around the tunnel for experiment 1. Particles that will be removed in subsequent frames are colored blue. (*Upper*) Simulation after equilibration at the specific frame. (*Lower*) Simulation after equilibration at a later frame. Column 1 shows a rendering of tunnel particles. Column 2 shows forces on tunnel particles. Column 3 shows a rendering of particles across the red plane in column 1. Column 4 shows forces through particles in column 3.

interparticle forces are identified as force chains, as defined in the introduction. Column 3 is a projection of particles onto the red plane in column 1. The set of particles projected is at distances of approximately three tunnel radii from the tunnel axis and two particle diameters from the plane. Such visualization reduces the dimension of the data, revealing patterns influenced by the tunnel axis. The final column presents the distribution of forces in this cross-section. In addition, a video of what an ant would see while traversing the green tunnel was compiled (Movie S3).

We make a couple inferences from these data. First, grain forces on the surface of the tunnel tend to be significantly less than that of grains positioned deeper into the bulk. In addition, surface forces are inclined to wrap around the axis of the tunnel rather than travel along it. This arching phenomenon will be explored in *Soil Arching*.

In Movie S2, the entire tunnel surface with its forces is rendered for 18 frames. The arching and force relaxation behaviors described above are even more apparent in the video. Next, we study these phenomena quantitatively by looking at the distribution of normal forces in the sample. As the tunnel head reaches a cross-section, contact forces decrease on the particles due to soil arching. The force between grains during slippage can be modeled by Coulomb friction (17). Therefore, the difficulty of removing a grain i is given by $\mu F_i^n + C$, where μ is the coefficient of friction between grains, C is the liquid bond strength that must be broken to remove a grain, and $F_i^n = \sum_j |F_{ij}^n|$ is the sum of the magnitude of normal forces on the grain, where F_{ij}^n is the jth contact force acting on particle i (drawing in Fig. 4). With lower normal forces, less pulling force is required to overcome friction between each particle and its neighbors. Furthermore, low-force grains are less structurally critical and can be supported through cohesive bonds. As ants remove particles at the tunnel head, the region of low force expands—granting the ants a larger set of loose grains to safely remove. As the tunnel head diameter is widened, the ants propagate the tunnel axis ever forward. Cohesive bonds and contact forces support force chain arches, which occur across the tunnel surface. These arches reform or strengthen as the tunnel is widened via ants "pruning" grains from the tunnel side walls. Tunnel widening dwindles at a given depth when a particular tunnel diameter is reached. In precis, we see that ants avoid removing high-force grains due in part to this high-force relaxation.

It is worth mentioning that the frustum-shaped container may provide additional stabilization due to the side walls. For instance, we see the largest tunnel—experiment 1—occurring along the sides. Nevertheless, arching behavior still occurs within the bulk, as evident from results for experiment 2 (Fig. 5) and detailed in *Soil Arching*.

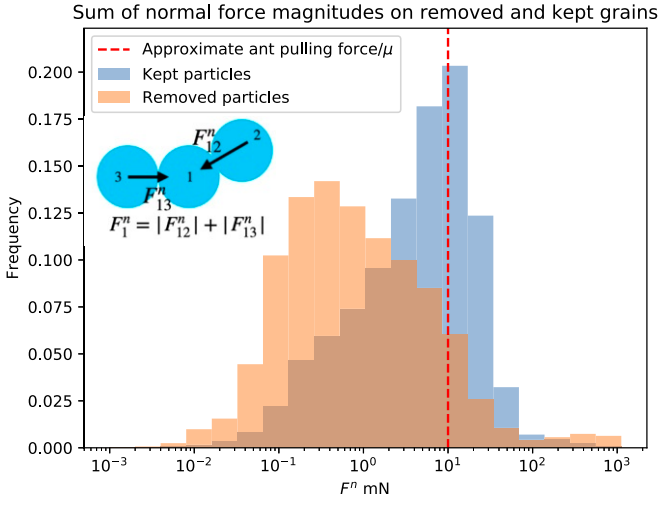

Fig. 4. Distributions of the sum of normal force magnitudes F^n for kept and removed particles across experiments 1 and 2, totaling 117,000 grains; the text has the F^n definition. The blue histogram is the distribution of F_i^n among all grains that are never removed at the frame before tunneling begins. The orange histogram is the distribution of the same parameter among particles at the frame immediately before said particle's removal. The approximate ant pulling force is plotted in red (6). Removed particles with F_i^n greater than the ant pulling force may be a consequence of model errors in predicting which particles are in force chains. The difference between the two distributions is statistically significant, with $P \ll 0.005$ under the Kolmogorov–Smirnov test. The dark area represents the overlap between the two histograms. (*Inset*) Schematic of normal contact forces acting on particle 1 from particles 2 and 3, and calculation of sum of normal force magnitude for particle 1 F_1^n.

Soil Arching. The effects described in the previous section are consequences of soil arching, which is considered in this section. As can be seen in Fig. 3 and Movie S1, force chains tend to wrap around the tunnel axis. It has been shown that the presence of a tunnel in soil will cause this "arching" effect not only on the tunnel's surface but also, in a larger zone centered around the tunnel axis (36). This effect could help explain why particles on the tunnel surface tend to transmit relatively lower interparticle forces.

Arching is defined by Terzaghi (37) as when "one part of a mass of soil yields while the remainder stays in place," causing a "shearing resistance within the zone of contact between the yielding and the stationary masses." Visually, arching often appears as force chains with an arch-like shape, emanating from a discontinuity like a void. Crucially, arching displaces load from the discontinuity to the surrounding area.

While a multitude of studies has analyzed stress fields around linear tunnels with tunnel axes perpendicular to gravity (23, 38, 39), there is a paucity of research on tunnels with variable axis directions and complex particle shapes—although recently linear angled tunnels have been considered in continuum models (40). Consequently, the nature of arching in our experiment was investigated.

It was hypothesized that arches would wrap about the tunnel axis, changing orientation with tunnel direction. To test this hypothesis, we again considered planes which pass through the fitted splines with normal vectors in the direction of the tunnel axis, see red plane in Fig. 3. For each plane we visualized the particles intersecting the plane, thereby forming a tunnel cross section. An example of a tunnel cross-section for experiment 2 is given in Fig. 5, where both the particles and the intergranular forces are visualized. Experiment 2 is the only instance when ants tunneled away from the container boundary and is more reminiscent of conditions found in nature. From inspection, forces at and near the tunnel surface have significantly decreased following excavation, in particular directly above the tunnel. Forces above the tunnel also tend to arch about the tunnel axis—displacing the large load from the soil weight away from the hole. Such arches act as a "stress shield," maintaining the low contact forces within their interior. This effect was recently studied by Fang et al. (32). Within the low stress zone, cohesive forces comparable with the weight of one grain are strong enough to support unloaded grains, allowing stable tunnels underneath pounds of earth. Therefore, arching occurs multiple layers deep into the material, shielding the vulnerable grains on the tunnel surface from forces that could trigger a collapse.

The histogram in Fig. 5 quantifies the effect of stress shielding. The blue histogram depicts F^n for grains that constitute the tunnel surface postexcavation (*SI Appendix*) at the frame before excavation begins. The orange plot corresponds to the distribution of F^n on the same grains after excavation. Clearly,

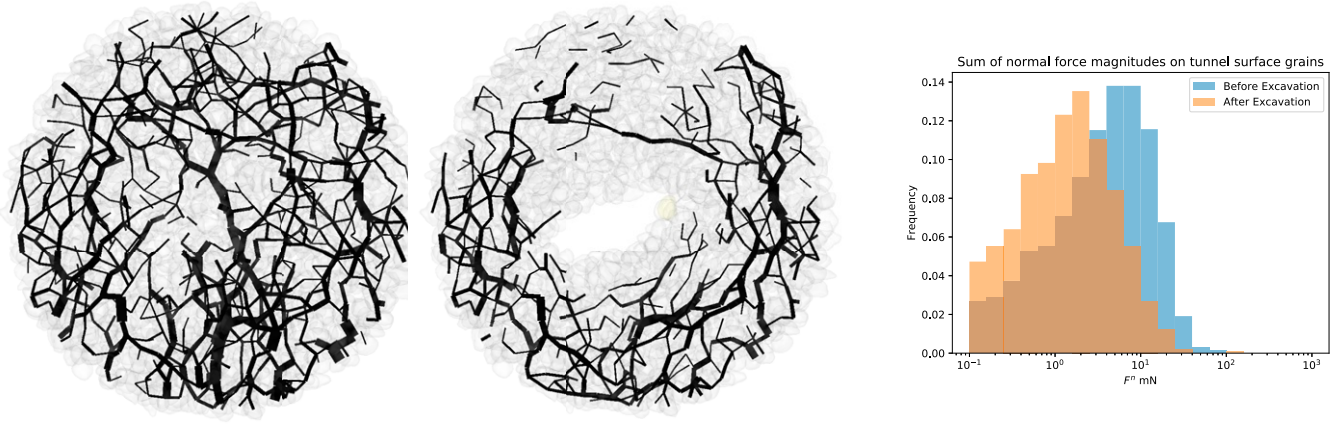

Fig. 5. Change in forces around the tunnel due to ant excavation for the green tunnel in experiment 2 within the bulk. (*Left*) Intergranular forces in a tunnel cross-section before excavation. (*Center*) Forces in the same cross-section after tunnel excavation. (*Right*) Distribution of F_n in particles that make the tunnel surface before and after excavation. The presence of the tunnel has reduced the stress in tunnel particles due to arching, with $P \ll 0.005$ under the Kolmogorov–Smirnov test.

excavation has reduced the load on the grains from the soil mass. To summarize, arches occurring within the soil form and strengthen during excavation. These arches reduce the load on particles at the tunnel surface. Thus, ants do not need to "know" which grains are in force chains before particle removal; by selecting any particle on the surface of the tunnel, ants have a high probability of avoiding a structurally critical grain.

Closure

We have provided evidence that a subterranean-nesting ant species tends to dig in piecewise linear tunnel segments. In addition, we demonstrated that the ants have a preference for removing smaller grains. Finally, we have demonstrated how ants can safely remove particles in a soil, even when digging below the soil surface, by benefiting from force redistributions via granular arching. We propose that granular arching provides an effective tunnel lining while also reducing load at the head of tunnel.

These results suggest that ants can maintain stable tunnels without needing to determine which exact particles are in force chains. Such findings are not at odds with how humans excavate: for instance, when utilizing a tunnel-boring machine. Nonetheless, ants achieve stability by gradually removing particles without the need for additional reinforcements—like tunnel linings and rock bolts. These results are applicable to a new class of palm-sized robots, which tunnel into soils (41, 42). Heuristics learned from our simulations could aid these robots in finding minimum energy paths through soils. Even more, the principles discovered here may have applicability toward hard rock mining, where tunnels consist of a handful of jointed rocks and are well suited to DEM analysis (43). It is the authors' intent to zoom out from the micromechanical world and to leverage this framework in the creation of automated excavation algorithms.

Data Availability. Experimental data and code have been deposited in CaltechDATA (code and data for "Unearthing real-time 3D ant tunneling mechanics"; https://doi.org/10.22002/D1.1996) (44).

ACKNOWLEDGMENTS. This work was supported by Army Grants W911NF-17-1-0212 and W911NF-19-1-0245. Laboratoire 3SR is part of the Laboratoire d'Excellence Mechanical and Process Engineering supported by Investissements d'Avenir Grant nANR-11-LABX-0030.

1. US Geological Survey, US mine production increasing, estimated value of $86.3 billion in minerals (2020). https://www.usgs.gov/news/us-mine-production-increasing-estimated-value-863-billion-minerals. Accessed 20 January 2021.
2. W. R. Tschinkel, Subterranean ant nests: Trace fossils past and future? *Palaeogeogr. Palaeoclimatol. Palaeoecol.* **192**, 321–333 (2003).
3. J. D. Frost *et al*., "Biologically-inspired insight into soil arching and tunnel stability from the topology of ant nests" in *19th International Conference on Soil Mechanics and Geotechnical Engineering* (2017).
4. D. Cassill, W. Tschinkel, S. Vinson, Nest complexity, group size and brood rearing in the fire ant, *Solenopsis invicta*. *Insectes Soc.* **49**, 158–163 (2002).
5. A. Khuong *et al*., Stigmergic construction and topochemical information shape ant nest architecture. *Proc. Natl. Acad. Sci. U.S.A.* **113**, 1303–1308 (2016).
6. D. Espinoza, J. Santamarina, Ant tunneling: A granular media perspective. *Granul. Matter* **12**, 607–616 (2010).
7. L. Scott, *Jenga*. Hasbro (1983).
8. J. Werfel, K. Petersen, R. Nagpal, Designing collective behavior in a termite-inspired robot construction team. *Science* **343**, 754–758 (2014).
9. R. L. Sousa, H. H. Einstein, Lessons from accidents during tunnel construction. *Tunn. Undergr. Space Technol.* **113**, 103916 (2021).
10. K. Siau, Z. Hyder, F.F.-H. Nah, "Use of artificial intelligence, machine learning, and autonomous technologies in the mining industry" in *Thirteenth Annual Midwest Association for Information Systems Conference* (2018).
11. D. Sivolella, *Off-World Mining in Space Mining and Manufacturing* (Springer, 2019), pp. 51–79.
12. D. Cassill, W. R. Tschinkel, S. B. Vinson, Nest complexity, group size and brood rearing in the fire ant, *Solenopsis invicta*. *Insectes Soc.* **49**, 158–163 (2002).
13. N. Gravish *et al*., Effects of worker size on the dynamics of fire ant tunnel construction. *J. R. Soc. Interface* **9**, 3312–3322 (2012).
14. N. Minter, N. Franks, K. Brown, Morphogenesis of an extended phenotype: Four-dimensional ant nest architecture. *J. R. Soc. Interface* **9**, 586–595 (2011).
15. N. Gravish, D. Monaenkova, M. A. Goodisman, D. I. Goldman, Climbing, falling, and jamming during ant locomotion in confined environments. *Proc. Natl. Acad. Sci. U.S.A.* **110**, 9746–9751 (2013).
16. D. Monaenkova *et al*., Behavioral and mechanical determinants of collective subsurface nest excavation. *J. Exp. Biol.* **218**, 1295–1305 (2015).
17. P. A. Cundall, O. D. L. Strack, A discrete numerical model for granular assemblies. *Geotechnique* **29**, 47–65 (1979).
18. A. S. Aleksiev, A. B. Sendova-Franks, N. R. Franks, The selection of building material for wall construction by ants. *Anim. Behav.* **73**, 779–788 (2007).
19. N. J. Minter, A. B. Sendova-Franks, N. R. Franks, Nest-seeking rock ants (*Temnothorax albipennis*) trade off sediment packing density and structural integrity for ease of cavity excavation. *Behav. Ecol. Sociobiol.* **67**, 1745–1756 (2013).
20. F. Radjai, M. Jean, J. J. Moreau, S. Roux, Force distributions in dense two-dimensional granular systems. *Phys. Rev. Lett.* **77**, 274–277 (1996).
21. J. Gili, E. Alonso, Microstructural deformation mechanisms of unsaturated granular soils. *Int. J. Numer. Anal. Methods Geomech.* **26**, 433–468 (2002).
22. R. P. Chen, Q. W. Liu, H. N. Wu, H. L. Wang, F. Y. Meng, Effect of particle shape on the development of 2D soil arching. *Comput. Geotech.* **125**, 103662 (2020).
23. Z. Y. Yin, P. Wang, F. Zhang, Effect of particle shape on the progressive failure of shield tunnel face in granular soils by coupled FDM-DEM method. *Tunn. Undergr. Space Technol.* **100**, 103394 (2020).
24. E. Azéma, F. Radjaï, Force chains and contact network topology in sheared packings of elongated particles. *Phys. Rev. E Stat. Nonlin. Soft Matter Phys.* **85**, 031303 (2012).
25. L. Li, E. Marteau, J. E. Andrade, Capturing the inter-particle force distribution in granular material using LS-DEM. *Granul. Matter* **21**, 43 (2019).

26. R. Kawamoto, E. Andò, G. Viggiani, J. E. Andrade, Level set discrete element method for three-dimensional computations with triaxial case study. *J. Mech. Phys. Solids* **91**, 1–13 (2016).
27. J. A. MacMahon, J. F. Mull, T. O. Crist, Harvester ants (*Pogonomyrmex* spp.): Their community and ecosystem influences. *Annu. Rev. Ecol. Syst.* **31**, 265–291 (2000).
28. D. H. Nguyen, E. Azéma, P. Sornay, F. Radjai, Effects of shape and size polydispersity on strength properties of granular materials. *Phys. Rev. E Stat. Nonlin. Soft Matter Phys.* **91**, 032203 (2015).
29. S. Lou, X. Jiang, P. J. Scott, Application of the morphological alpha shape method to the extraction of topographical features from engineering surfaces. *Measurement* **46**, 1002–1008 (2013).
30. V. Richefeu, M. S. El Youssoufi, F. Radjaï, Shear strength properties of wet granular materials. *Phys. Rev. E Stat. Nonlin. Soft Matter Phys.* **73**, 051304 (2006).
31. M. R. Shaebani, T. Unger, J. Kertész, Extent of force indeterminacy in packings of frictional rigid disks. *Phys. Rev. E Stat. Nonlin. Soft Matter Phys.* **79**, 052302 (2009).
32. Y. Fang, L. Guo, M. Hou, Arching effect analysis of granular media based on force chain visualization. *Powder Technol.* **363**, 621–628 (2020).
33. R. Kawamoto, E. Andò, G. Viggiani, J. E. Andrade, All you need is shape: Predicting shear banding in sand with LS-DEM. *J. Mech. Phys. Solids* **111**, 375–392 (2018).
34. D. O. Potyondy, P. Cundall, A bonded-particle model for rock. *Int. J. Rock Mech. Min. Sci.* **41**, 1329–1364 (2004).
35. M. Cha, J. C. Santamarina, Localized dissolution in sediments under stress. *Granul. Matter* **21**, 79 (2019).
36. R. Chen, L. Tang, D. Ling, Y. Chen, Face stability analysis of shallow shield tunnels in dry sandy ground using the discrete element method. *Comput. Geotech.* **38**, 187–195 (2011).
37. K. Terzaghi, *Theoretical Soil Mechanics* (John Wiley & Sons, Ltd., 1943), pp. 66–76.
38. L. Wu, X. Zhang, Z. Zhang, W. Sun, 3D discrete element method modelling of tunnel construction impact on an adjacent tunnel. *KSCE J. Civ. Eng.* **24**, 657–669 (2020).
39. C. Lee, B. Wu, H. Chen, K. Chiang, Tunnel stability and arching effects during tunneling in soft clayey soil. *Tunn. Undergr. Space Technol.* **21**, 119–132 (2006).
40. O. P. Vitali, T. B. Celestino, A. Bobet, Analytical solution for tunnels not aligned with geostatic principal stress directions. *Tunn. Undergr. Space Technol.* **82**, 394–405 (2018).
41. R. Borela, J. Frost, G. Viggiani, F. Anselmucci, Earthworm-inspired robotic locomotion in sand: An experimental study with x-ray tomography. *Géotech. Lett.* **11**, 66–73 (2021).
42. A. Sadeghi, A. Mondini, B. Mazzolai, Toward self-growing soft robots inspired by plant roots and based on additive manufacturing technologies. *Soft Robot.* **4**, 211–223 (2017).
43. C. Boon, G. Houlsby, S. Utili, Designing tunnel support in jointed rock masses via the dem. *Rock Mech. Rock Eng.* **48**, 603–632 (2015).
44. R. Buarque De Macedo, Code and Data for 'Unearthing real time 3D ant tunneling mechanics' (Version 1.0) [Data set]. CaltechDATA. https://doi.org/10.22002/D1.1996. Deposited 10 June 2021.